NANO LETTERS

pubs.acs.org/NanoLett Letter

MetaHeat: Programmable Photothermal Heating in Complex Media with Inverse-Designed Metasurfaces

Homayra T. Mumu,[†] Yujie Luo,[†] Joseph Kangas, John Bischof, Cari Dutcher, and Ognjen Ilic*

Cite This: https://doi.org/10.1021/acs.nanolett.6c02380 Read Online

ACCESS | Metrics & More | Article Recommendations | SI Supporting Information

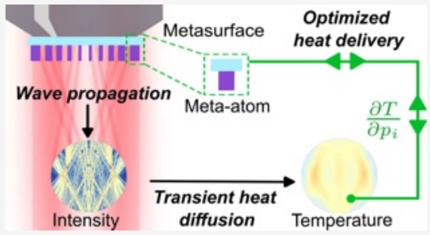

ABSTRACT: Precise spatial control of light-induced heating is critical across photothermal applications ranging from laser therapies to materials processing yet remains difficult in the presence of complex refractive interfaces. For example, laser warming of cryopreserved specimens requires uniform, rapid heating, but refractive distortions produce damaging thermal gradients that compromise viability. We present MetaHeat, a metasurface-based wavefront engineering framework for programmable photothermal heating in complex media. MetaHeat addresses the coupled challenge of light propagation and subsequent heat transport by combining angular-spectrum wave propagation with transient diffusion in a unified, differentiable framework. Applied to laser warming, MetaHeat navigates a high-dimensional metasurface design space—with thousands of meta-atoms—constructing wavefronts that suppress hot and cold spots, reducing spatial temperature variance by over an order of magnitude (≈31×) in a representative target. We observe similar improvements in additional geometries, suggesting the approach is general and provides a route to programmable photothermal heating in complex refractive media.

KEYWORDS: *meta-optics, photothermal heating, wavefront engineering, inverse design, laser warming*

Controlling where light deposits energy is a central challenge in photothermal systems, because the spatial distribution of optical intensity directly determines the resulting temperature field. This need arises across a wide range of applications: in some, focused laser beams are used to drive highly localized thermal processes such as melting, cutting, welding,[1,2] and laser-based additive manufacturing;[3] in others, shaped light fields are required for targeted energy delivery in photothermal applications, such as cancer therapy,[4−6] laser treatment,[7−9] microsurgery,[10] and cryopreservation.[11] Related challenges also arise in applications such as optogenetics and neural stimulation, where light needs to be focused through highly scattering brain tissue to activate targeted neurons with high spatial specificity.[12,13] Across this diverse range of examples, the common requirement is not just the delivery of optical intensity, but the ability to prescribe and maintain a desired spatial pattern of energy deposition within the target (Figure 1a).

However, in many important applications, it is difficult to obtain the desired spatial intensity profile due to the presence of multiple refracting interfaces. A particularly compelling example is laser warming of cryopreserved biological samples, which requires highly uniform and rapid heating. Uniform heating is crucial because the critical warming rate (CWR) must be exceeded everywhere in the sample to prevent intracellular ice formation that causes cell death. Ice nucleated at any sub-CWR site grows rapidly, compromising specimen viability.[14] In this setting, light propagates through a geometrically and optically complex target with multiple interfaces (droplet to air boundary, specimen boundaries, intracellular boundaries, etc.). These interfaces strongly distort the incident wavefront, generating hot and cold regions (Figure 1b) that translate into nonuniform heating.[15,16] Because these thermal gradients are difficult to suppress directly, one strategy has been to inject scattering nanoparticles into the droplet and biological specimen.[15,17−19] However, such approaches can suffer from poor redistribution of particles, loss of directionality due to randomized orientation, and concerns related to cytotoxicity and long-term stability.[18−21]

Beyond such specimen-modification strategies, a range of optical platforms can also be used to shape spatial wavefronts, including microlens arrays,[6,22−24] freeform optics,[25−30] and programmable devices such as liquid-crystal spatial light modulators,[31−33] digital micromirror devices,[34,35] and deformable mirrors.[36−38] However, although such methods have been used to shape beams in free space or at designated target planes, the challenge in many photothermal applications is more demanding because the target itself reshapes the wavefront. Addressing this challenge requires an inverse-design framework that directly links the incident optical wavefront to the resulting thermal field. For programmable heating, the

Received: May 17, 2026
Revised: July 29, 2026
Accepted: July 31, 2026

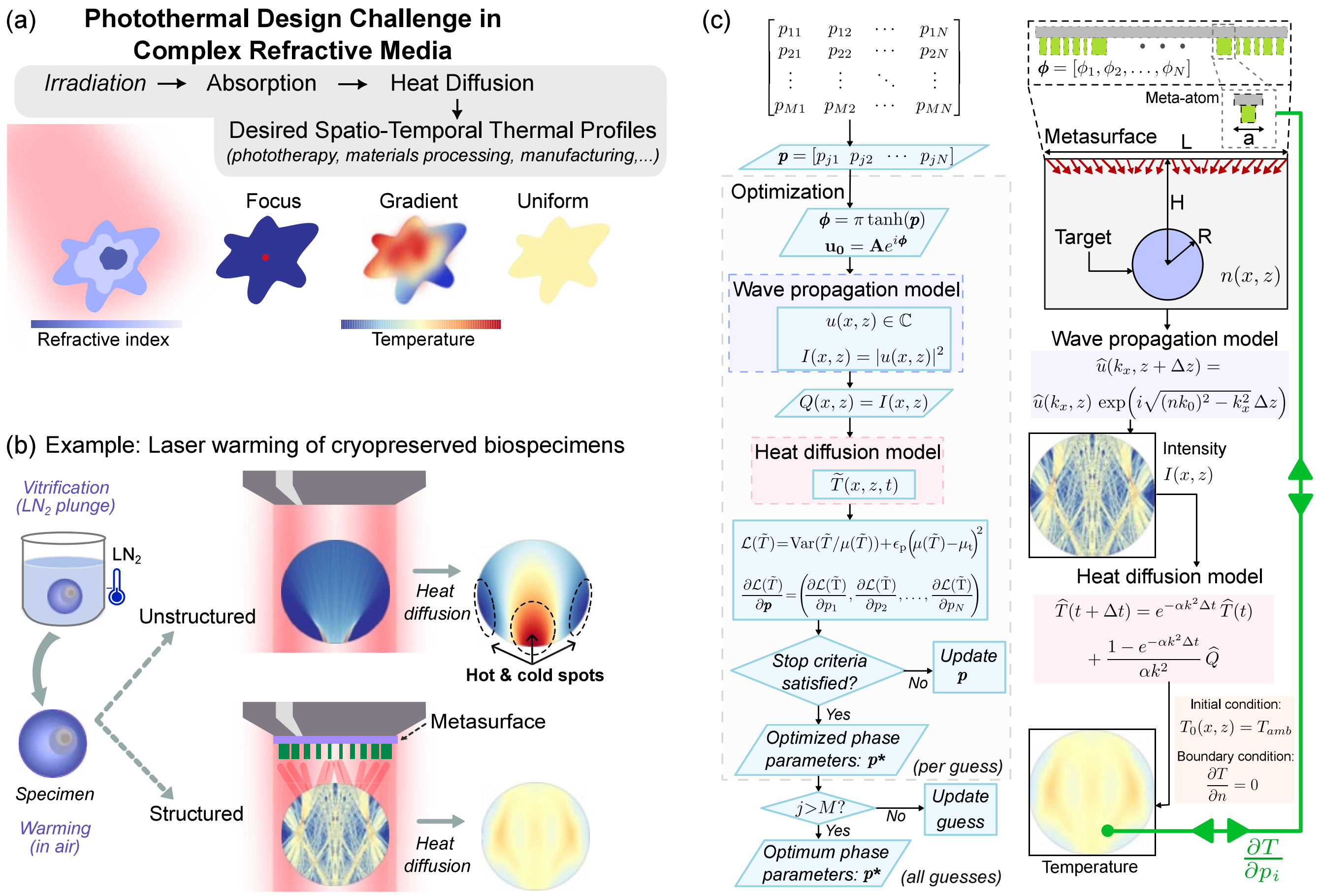

Figure 1. Photothermal heating challenge and the MetaHeat framework. (a) Schematic of the photothermal design challenge: irradiation propagates through a system with complex refractive interfaces to produce a spatiotemporal heat deposition pattern, but achieving prescribed thermal patterns is difficult due to refractive distortion at multiple interfaces. (b) A representative example: in laser thawing of cryopreserved biospecimens, successful warming requires rapid and highly uniform internal heating; however, under unstructured irradiation, refractive interfaces distort the incident wavefronts (the self-lensing effect[15,16]), forming hot and cold regions that damage the specimen and compromise viability. In contrast, a metasurface-structured wavefront is designed to account for both refraction and subsequent heat diffusion, yielding a substantially more uniform temperature field. (c) The MetaHeat photonic-thermal modeling chain maps metasurface parameters to the time-evolved temperature field. Meta-atoms locally control the phase of the wavefront that evolves across the domain to produce the intensity distribution $|u(\boldsymbol{x})|^2$, which acts as a source term $Q(\boldsymbol{x})$ in the heat diffusion equation. The chain is end-to-end differentiable, enabling direct gradient computation (e.g., $\partial T/\partial p_i$ for each meta-atom i) for efficient inverse design.

relevant design objective is not simply optical focusing or homogenization in free space, but the generation of a prescribed temperature response inside the matter after accounting for *both* refraction at all interfaces *and* time-dependent heat diffusion throughout the target. This is inherently a coupled photonic-thermal challenge, and its practical solution depends on a framework that accurately captures the underlying physics while remaining computationally efficient to optimize wavefronts with many degrees of freedom.

Here, we present a metasurface-based wavefront engineering framework for programmable photothermal heating in complex media ("MetaHeat"). Our approach combines an angular-spectrum wave propagation model with a Fourier-domain transient heat diffusion model to establish a direct, end-to-end differentiable mapping from metasurface phase parametrization to the time-evolved temperature field. MetaHeat enables efficient inverse design of large metasurfaces (with thousands of independently tunable meta-atoms) by directly linking each meta-atom's phase to the resulting thermal response. Applying this strategy to the problem of uniform warming of cryopreserved samples, we demonstrate that wavefronts can be structured to suppress the internal hot and cold spots that arise under under conventional irradiation (Figure 1b and Table S1) Although laser warming provides a motivating example here, MetaHeat is general and offers a route to programmable heat delivery in optically complex media.

Figure 1c illustrates the MetaHeat framework and the overall metasurface design process. Let $\mathbf{p} = [p_1, p_2, ..., p_N] \in \mathbb{R}^N$ denote the vector of unconstrained design variables, where each p_i corresponds to a single meta-atom in the metasurface. We map $\mathbf{p}$ to a bounded phase profile $\boldsymbol{\phi}$ in a manner that avoids discontinuities due to 2π wrapping, namely, $\phi_i = \pi \tanh(p_i)$, where $\phi_i \in (-\pi, \pi)$. This smooth bounding operation preserves differentiability while enforcing a physically reasonable phase range for each design meta-atom. Our assumption is that each meta-atom in the metasurface has a spatial size of a, which is also the period of the meta-atom. This leads to the total number of design variables equal to $N = L/a$, where L is the size of the metasurface.

Next, the set of independent meta-atom design variables p_i (or, equivalently, meta-atom phases ϕ_i) is mapped to the

https://doi.org/10.1021/acs.nanolett.6c02380
Nano Lett. XXXX, XXX, XXX−XXX

metasurface aperture and a wave propagation solver is used to calculate the complex field throughout the propagation domain. First, the discrete phase set ϕ_i is upsampled to a finer pixel grid commensurate with the resolution of the wave propagation solver. If $\phi(x)$ denotes the interpolated/upsampled phase profile, the aperture field at the metasurface plane $z = 0$ can be expressed as $u_0(x) = A(x)\, e^{i\phi(x)}$. Given the aperture field $u_0(x)|_{z=0}$, the wave propagation method solves the Helmholtz equation by decomposing the field into plane waves.[39] In the angular spectrum formulation, the field is evolved along the propagation direction as

$$u(x, z + \Delta z) = \mathcal{P}[u(x, z), n] = \mathcal{F}^{-1}\{\mathcal{F}\{u(x, z)\}\cdot H(n, \Delta z)\} \tag{1}$$

where $\mathcal{P}$ is the propagation operator expressed in terms of the spatial Fourier transform $\mathcal{F}$, and $H(n, \Delta z) = \exp(i\sqrt{(nk_0)^2 - k_x^{\,2}}\,\Delta z)$, which is the propagation transfer function over transverse spatial frequencies k_x. Here, $k_0 = 2\pi/\lambda$ is the free-space wavenumber and n is the refractive index. In our case, the presence of a target object leads to a nonhomogeneous refractive index profile $n(x, z)$. To account for refractive index nonhomogeneity, each transverse slice can be decomposed into regions of unique refractive indices. If there are K unique refractive index values $(n_1, n_2, ..., n_K)$ in a slice of the propagation domain, the field propagator is augmented as

$$u(x, z + \Delta z) = \sum_{j=1}^{K} M_j(x)\cdot\mathcal{P}[u(x, z), n_j] \tag{2}$$

where $M_j(x)$ is a binary mask, i.e., $M_j(x) = 1$ if $n(x, z) = n_j$ and 0 otherwise. This propagator neglects lateral coupling across index boundaries and is most appropriate when forward propagation dominates, index variations are resolved with sufficiently small Δz, and strong resonant recirculation is absent. Its suitability for the present geometries is supported by direct comparison with full-wave FDTD simulations in Figure S2. The end result is the mapping of the meta-atom phase distribution $\boldsymbol{\phi}$ to the evolved field $u(x, z)$ over the irradiated target object.

Once the irradiated field is known, the intensity of that field becomes a source in the heat diffusion equation (Figure 1c). Specifically, the time-dependent heat diffusion inside the target object can be expressed as

$$\frac{\partial T(x, z, t)}{\partial t} = \alpha\nabla^2 T(x, z, t) + Q(x, z, t) \tag{3}$$

where T is the temperature field, α is the material thermal diffusivity, and Q is the source term. In standard models of electromagnetic-induced heating, the local heat generation rate is assumed to be proportional to the electromagnetic power absorbed by the material, which, in turn, is proportional (for linear media) to the electromagnetic field intensity. Therefore, we express the spatial heating source term as $Q(x, z, t) = \gamma|u(x, z, t)|^2$, where the constant of proportionality γ is a material-dependent coefficient determined by the absorption properties (e.g., the imaginary part of the permittivity or an effective absorption coefficient). Next, from the standpoint of computational efficiency and automatic differentiability, we reformulate the time-dependent heat diffusion equation (3) in Fourier space as

$$\hat{T}(k_x, k_z, t + \Delta t) = e^{-\alpha k^2\Delta t}\cdot\hat{T}(k_x, k_z, t) + \frac{1 - e^{-\alpha k^2\Delta t}}{\alpha k^2}\cdot\hat{Q}(k_x, k_z, t) \tag{4}$$

where $\hat{T}$ and $\hat{Q}$ are the Fourier transforms of the spatial temperature field $T(x, z)$ and spatial heating field $Q(x, z)$, and $k^2 = k_x^{\,2} + k_z^{\,2}$ the corresponding Fourier wavenumbers. In the Supporting Information, we provide the derivation of eq 4, along with the details of implementing the heat diffusion equation boundary conditions at the target object interface. Because laser warming occurs over a millisecond time scale while the sample remains predominantly vitrified, heat transport is dominated by conduction, whereas internal convection and external convective and radiative heat losses are negligible relative to the volumetric laser energy deposited within the specimen. Once the temperature is time-stepped in Fourier space according to eq 4, the real-space temperature field can be recovered as $T(x, z, t) = \mathcal{F}^{-1}\{\hat{T}(t)\}$. In particular, $T(x, z, t)$ represents the temperature *rise* relative to the initial uniform temperature T_0. For clarity, we henceforth refer to temperature rise as $\tilde{T}(x,z,t)$.

A key aspect of our approach is to make the entire modeling chain outlined in Figure 1c—namely, $\mathbf{p} \to \boldsymbol{\phi} \to u_0(x)|_{z=0} \to u(x, z) \to Q(x, z) \to T(x, z, t)$—differentiable and compatible with modern autodifferentiation implementations. Autodifferentiable modeling refers to the ability to compute exact derivatives of model outputs with respect to all input parameters through algorithmic differentiation, rather than finite differences.[40,41] Developed to train neural networks by efficiently propagating gradients through complex computational chains, these techniques now underlie major machine learning libraries and programming languages, such as Python/Jax, Julia, and others.[42−44] This approach is aligned with recent inverse-design efforts in thermal photonics, including structures optimized to achieve prescribed spectral absorption, reflection, and emission properties.[45,46] In our case, because all operations (FFT, pointwise multiplication, inverse FFT, etc.) are differentiable, the gradient chain of the full map $\frac{\partial T}{\partial p} = \frac{\partial T}{\partial Q}\cdot\frac{\partial Q}{\partial u}\cdot\frac{\partial u}{\partial u_0}\cdot\frac{\partial u_0}{\partial \phi}\cdot\frac{\partial \phi}{\partial p}$ directly relates the spatial temperature field to meta-atom design variables p. Correspondingly, for any figure of merit that is a scalar function of temperature $\mathcal{L}(T)$ (e.g., temperature uniformity), the gradient with respect to each meta-atom design variable (i.e., each meta-atom phase) is computed via backpropagation $\frac{\partial \mathcal{L}}{\partial p}$. Reverse-mode autodifferentiation is closely related to the adjoint method and can be interpreted as automatically constructing the discrete adjoint. The advantage in the present framework is the ability to obtain gradients through a multistage photonic-thermal computation chain without the need to manually derive separate adjoint formulations for each stage. Unlike conventional one-sided finite-difference approaches, which require $N + 1$ simulations for a system with N parameters (and $2N$ for central differences), autodifferentiability provides all gradients using a single forward pass followed by a backward pass, at a total computational cost on the order of two simulations, independent of the number of parameters N. This distinction is essential for our metasurface design. A metasurface may comprise thousands of meta-atoms, each with an independently tunable phase, resulting in thousands of design variables. Under these conditions, finite-difference gradient estimation

https://doi.org/10.1021/acs.nanolett.6c02380
Nano Lett. XXXX, XXX, XXX−XXX

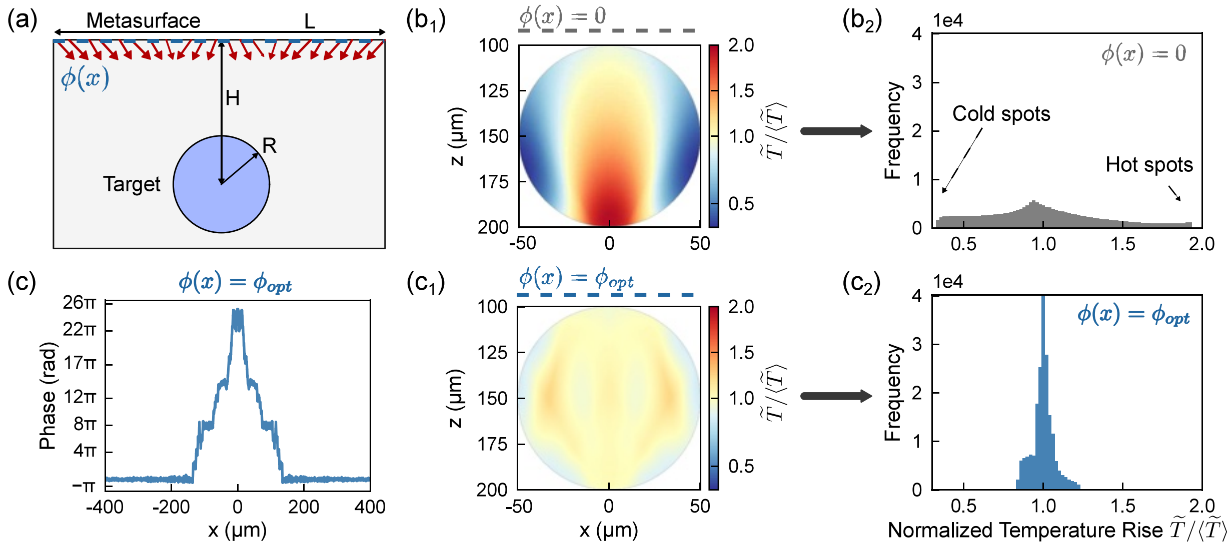

Figure 2. (a) Optimizing metasurface phase profile for heating uniformity: spherical target. Unstructured wavefront irradiation: (b_1) resulting time-evolved temperature field and (b_2) its frequency distribution. Optimally structured metasurface wavefront phase profile: (c_1) resulting time-evolved temperature field and (c_2) its frequency distribution. Normalized temperature corresponds to the average temperature. Here, $R = 50$ μm, $H = 150$ μm, and refractive index $n = 1.5$. Further optimization additionally improves temperature uniformity (Table S1 and Figure S5) but increases sensitivity to uncertainties in the target offset and refractive index (Figure S6).

becomes computationally prohibitive, whereas the MetaHeat framework of Figure 1c remains tractable and well-suited for the design of metasurfaces for coupled photonic-thermal applications, such as light-induced heating.

Figure 2 illustrates the MetaHeat design strategy for achieving uniform light-induced heating within a spherical object. We consider a metasurface aperture positioned at a distance $H = 150$ μm from an object of radius $R = 50$ μm, refractive index $n = 1.5$, and thermal diffusivity $\alpha = 0.127$ mm^2/s; the wavelength of the incident beam is $\lambda = 1064$ nm (Figure 2a). These parameter values are motivated by prior studies on laser-induced thawing of cryopreserved samples.[15] As a baseline case, we first examine unstructured irradiation, corresponding to a spatially constant phase $\phi = 0$ across the aperture plane. Figure $2b_1$ shows the resulting temperature rise $\tilde{T}$ after a heating duration of $t_s = 2$ ms (a characteristic heating time[17,47,48]). Since our focus is on the temperature distribution within the object, it is informative to plot the normalized temperature rise $\tilde{T}(x, z)/\langle\tilde{T}\rangle$, where $\langle\tilde{T}\rangle$ denotes the average temperature rise within the object, namely, $\langle\tilde{T}\rangle = \int_\Omega \tilde{T}\, dA/\int_\Omega dA$. This is because the average temperature rise is proportional to the incident optical power and can thus be rescaled without altering the normalized temperature distribution. The temperature rise shown in Figure $2b_1$ indicates a pronounced hot spot in the bottom region and cold spots along the sides, reflecting the self-focusing effect of a spherical interface (Figure 1b). The variation in temperature is substantial: the rise in the hot region is nearly six times larger (5.9×) than in the cold regions (for example, if the incident beam power is adjusted such that the average temperature rise within the object is 50 °C, the temperature rise in hot spots is close to 100 °C, whereas the temperature rise in the coldest regions remains below 20 °C). Figure $2b_2$ shows the corresponding histogram of the temperature rise distribution.

We proceed to design the metasurface phase profile that minimizes the nonuniformity functional $\mathcal{L}(\tilde{T}) = \mathrm{Var}(\tilde{T}/\mu(\tilde{T})) + \epsilon_p(\mu(\tilde{T}) - \mu_{target})^2$. The first term denotes the variance of normalized temperature rise $\tilde{T}$ over the object domain Ω; it directly quantifies nonuniformity and is the primary quantity we seek to minimize. The second term sets the target mean penalty, where $\mu(\tilde{T}) = \langle\tilde{T}\rangle = \int_\Omega \tilde{T} dA/\int_\Omega dA$ is the mean. Without the target mean penalty term, the optimizer could trivially achieve zero variance by deflecting all light away from the object. Setting ϵ_p and μ_{target} based on a baseline design anchors the optimization to physically meaningful power levels. Finally, we minimize $\mathcal{L}(\tilde{T})$ with respect to design variables $\boldsymbol{p}$ using the L-BFGS gradient-based optimization algorithm, with gradients $\partial\mathcal{L}(\tilde{T})/\partial\boldsymbol{p}$ computed via automatic differentiation. Figure 2c shows the optimized phase profile $\phi_{opt}(x)$. We assume a meta-atom size of $a = 0.4$ μm, corresponding to a total of $N = 2,000$ meta-atoms across the aperture.

Similar to Figure $2b_1$, which showed the temperature rise within the object for an unstructured phase profile (equivalent to the absence of the metasurface), Figure $2c_1$ shows the temperature rise for the optimized phase profile. The resulting temperature rise is significantly more uniform and tightly clustered around the average value. As before, we plot the temperature rise normalized by the spatially averaged temperature rise. From the histogram of the temperature distribution (Figure $2c_2$), we observe that 83.4% of the object lies within 10% of the average temperature rise. This means that, for example, if the incident beam power is adjusted such that the average temperature rise is 50 °C, then 83.4% of the object experiences a temperature rise within 45–55 °C, with the coldest (hottest) spot at 42 °C (61 °C) temperature rise. Overall, temperature variance is approximately 31 times lower than for unstructured irradiation, corresponding to ≈5.6× reduction in the standard deviation of the normalized temperature distribution. Additional optimization can further improve temperature uniformity, as shown in Table S1 and Figure S5 (e.g., variance reduction of ≈91×), but increases sensitivity to uncertainties in the target offset and refractive index (Figure S6).

https://doi.org/10.1021/acs.nanolett.6c02380
Nano Lett. XXXX, XXX, XXX−XXX

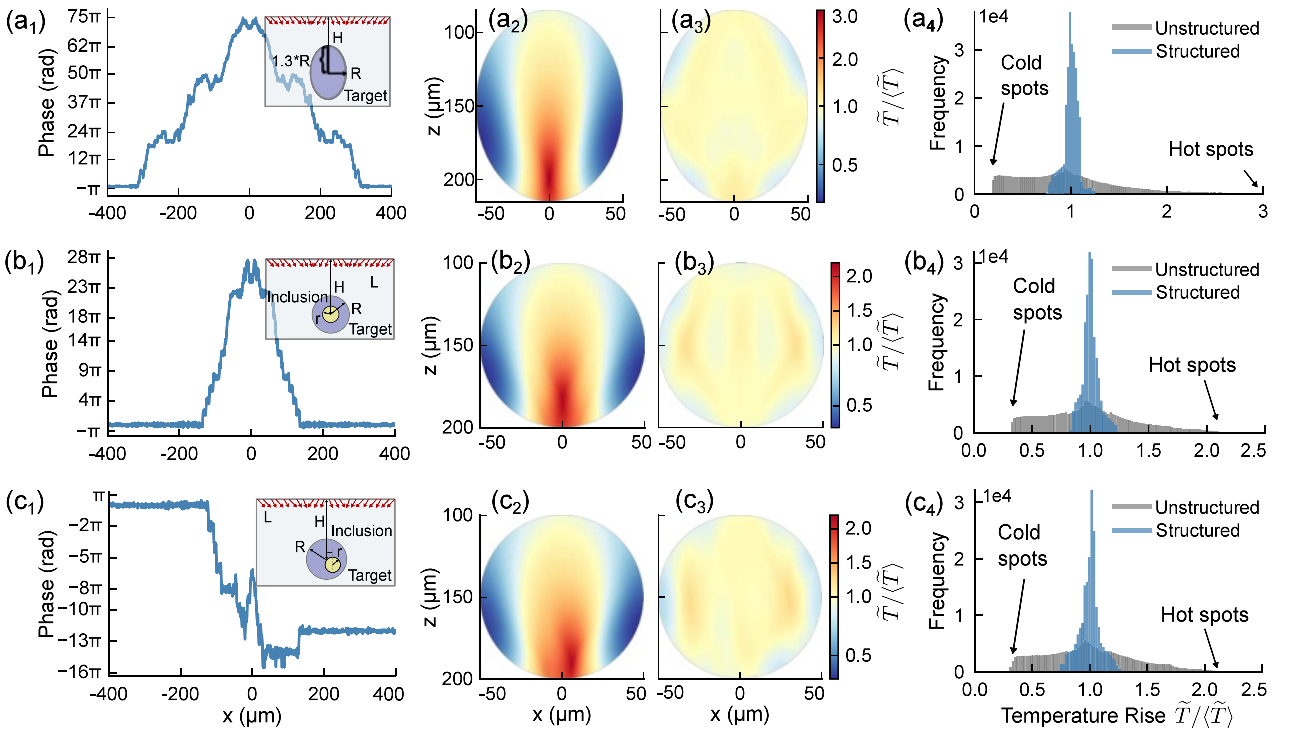

Figure 3. Optimizing metasurface profile for heating uniformity in related geometries. (a_{1-4}) *Elliptical target*: (a_1) optimal phase profile; time-evolved temperature field for (a_2) unstructured and (a_3) structured (optimized) wavefront; (a_4) temperature histogram. (b_{1-4}) *Spherical target with centered inclusion*: (b_1) optimal phase profile; time-evolved temperature field for (b_2) unstructured and (b_3) structured wavefront; (b_4) temperature histogram. (c_{1-4}) *Spherical target with off-centered inclusion*: (c_1) optimal phase profile; time-evolved temperature field for (c_2) unstructured and (c_3) structured wavefront; (c_4) temperature histogram.

In Figure 3, we demonstrate that the same approach can be applied to a target object with an arbitrary shape. As a first extension, we consider an ellipse-like object with a height of H = 130 μm and diameter D = 100 μm, with results shown in panels a_{1-4} in Figure 3. The optimized phase profile resembles that of the spherical case (Figure 2c), though here the optimized aperture is wider. This is consistent with the elongated geometry of the ellipse, which benefits from a broader aperture to achieve improved uniformity. As in the spherical case, an unstructured phase profile produces a self-focusing effect, resulting in a hot region along the central axis and two colder regions along the sides (Figure 3a_2). In contrast, the optimized phase profile yields a much more uniform temperature distribution (Figure 3a_3). From the histogram of the two temperature profiles (Figure 3a_4), we observe that the unstructured phase profile produces a broad distribution: if the average temperature rise is 50 °C, the cold spots have minimum temperature of 9 °C while the hotspots reach 150 °C. In contrast, the optimized phase profile yields a much more uniform distribution, with 85% of the object domain lying within 10% of the average temperature rise.

Next, we investigate the case of an object with an inclusion as an example of a nonhomogeneous refractive index profile inside a target object (Figure 3b_{1-4}). The concentric inclusion has a size of r = 20 μm and refractive index of n_i = 1.8. For unstructured irradiation, the presence of the inclusion leads to increased self-focusing, producing a more pronounced temperature rise contrast between the hot and cold regions. The optimized metasurface phase profile is again able to achieve a more uniform temperature profile. The histogram in Figure 3b_4 shows that 85.4% of the object domain lies within 10% of the average temperature rise. Finally, we shift the position of the inclusion within the object to create a nonsymmetric irradiation target (Figure 3c_{1-4}). In this case, the optimized metasurface phase profile is no longer symmetric. Nevertheless, its ability to improve heating uniformity is maintained. As we see from the histogram of the temperature profiles, 76.5% of the object domain lies within 10% of the average. Improvements in variance, standard deviation, and temperature range, along with additional optimization results, are summarized in Table S1.

To better understand the impact of the metasurface on transient heating, we compare the temporal evolution of the temperature fields for the case of the unstructured irradiation without a metasurface and structured irradiation with the metasurface (Figure 4). The temperature distributions are evaluated at four time points (0.5, 1, 2, and 4 ms) with the irradiation source continuously on during this interval. In each case, the temperature rise is normalized to the average temperature rise at t = 2 ms to enable direct comparison across time. When the metasurface is not present (Figure 4a_{1-4}), heat diffusion progressively broadens the temperature distribution during the heating process. As time increases, the contrast between hotter and colder regions becomes more pronounced, as quantified in Figure 4c, where the temperature spread continues to grow. In contrast, when the metasurface is present (Figure 4b_{1-4}), the initially localized temperature distribution peak evolves differently. Although thermal diffusion still occurs, the temperature profile remains significantly narrower over time, indicating improved spatial confinement and reduced thermal nonuniformity compared to the nonmetasurface case. Figure 4d visualizes the temporal evolution of this comparatively narrow temperature distribution made possible by the optimized metasurface.

https://doi.org/10.1021/acs.nanolett.6c02380
Nano Lett. XXXX, XXX, XXX−XXX

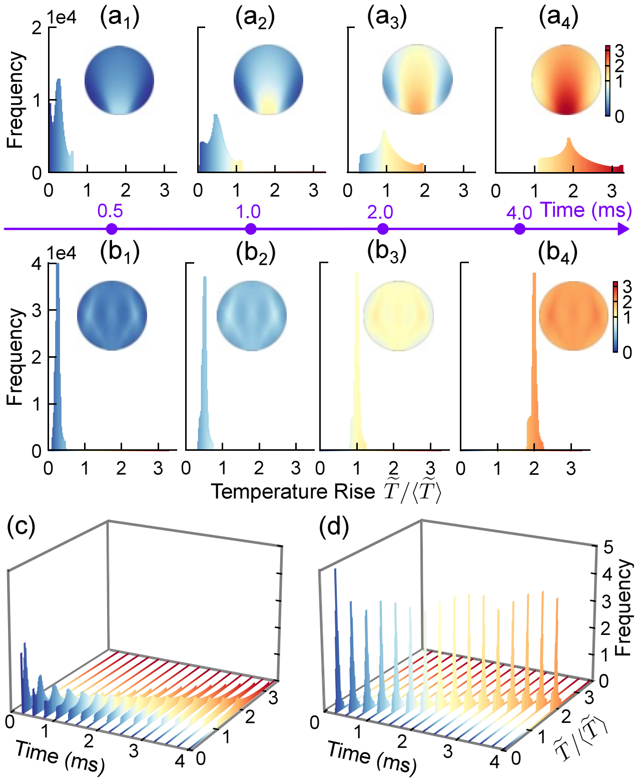

Figure 4. Spatiotemporal temperature distribution and corresponding histograms during laser heating. (a_{1-4}) Histograms for unstructured irradiation at t = 0.5, 1, 2, and 4 ms show progressive broadening of the temperature distribution as heat diffuses through the medium. (b_{1-4}) Histogram evolution of structured wavefront irradiation at the same time points shows a consistently narrow temperature distribution throughout the heating period. Evolution of temperature distribution for unstructured (c) and optimally structured (d) irradiation.

In summary, this work demonstrated that metasurfaces can be used to structure irradiation wavefronts to achieve uniform light-induced heating within objects whose complex refractive interfaces would otherwise produce pronounced hot and cold spots. This was made possible by a differentiable photonic-thermal framework that combined an angular spectrum wave propagation model with a Fourier-domain transient heat diffusion model ("MetaHeat"), establishing a direct mapping from the metasurface phase parametrization to the spatial temperature rise within the target object. In this manner, the temperature distribution at any point within the object could be traced back to each individual meta-atom through the gradient $\partial\tilde{T}/\partial p_i$, enabling an efficient pathway for metasurface design. Applying this approach to a representative spherical target, we showed that the spatial temperature variance can be substantially reduced, with similar improvements observed in related geometries (e.g., elliptical target, target with embedded inclusion). We note that MetaHeat can be seen as complementary to nanoparticle-assisted laser warming. Nanoparticles can enhance absorption and, in some regimes, scattering, but scattering effects are limited by uncontrolled particle orientation, which can prevent deterministic correction of refractive hot and cold spot patterns. On the other hand, MetaHeat reshapes the incident wavefront before absorption occurs, directly compensating for refractive distortions. The two approaches can be combined, with nanoparticles providing enhanced absorption and MetaHeat optimizing the spatial profile of optical energy delivery.

We discuss several relevant extensions. This work focuses on a concept-proof analysis in two dimensions (2D) and the reported numerical values should not be interpreted as quantitative predictions for full 3D targets. Nevertheless, while the quantitative results would change in 3D, the coupled differentiable, photonic-thermal formulation is not intrinsically limited to 2D: a 3D implementation would replace the 2D optical and temperature fields with their 3D analogs and the metasurface phase profile with a two-dimensional phase mask. The propagation of the wavefront within the medium is governed by the level of absorption. Here, we consider regimes in which the incident wavefront can propagate through the object and interact with all internal interfaces. As shown in Figure S1, increased absorption modifies the optimal metasurface design, indicating that the solution is, in general, absorption-dependent. In the limit of strong absorption, the incident wavefront may not reach the opposite side of the object, in which case bidirectional irradiation (e.g., front and back side) may be required, an extension that could be incorporated within the present framework.

Experimentally, the framework could be validated in stages: first, metasurface-generated intensity profiles could be recorded in photochromic or photobleaching polymer microstructures to verify the predicted optical energy distribution; next, temperature-sensitive dyes or thermochromic reporter materials could be used to record transient temperature rise and test the predicted improvement in thermal uniformity. Likewise, the angular spectrum method employed here is most appropriate for scenarios with a dominant forward-propagating field and does not capture strong or resonant light recirculation (e.g., in an optical cavity). This is not expected to be a significant limitation for photothermal heating in biological media, which are sufficiently incoherent and nonresonant at the relevant wavelengths. Consistent with this, comparison with full-wave simulations supports the validity of our approach. Figure S2 shows the simulated wavefront evolution obtained with the finite-difference time-domain (FDTD) method, which solves the full Maxwell's equations subject to discretization limits set by the spatial and temporal resolution.[49] Similarly, Figure S3 shows the temperature profile computed using a finite-difference scheme to solve the heat diffusion equation, serving as a reference benchmark and showing strong agreement. Having validated the intensity distribution against FDTD and the temperature field against the finite-difference heat solver, we then designed an example TiO_2 metasurface implementing the optimized phase profile (Figure 2c) for uniform heating of a cylindrical target. Figure S4 shows that the resulting intensity and temperature distributions are in good agreement with those predicted by the MetaHeat model.

Finally, the thermal model employed here assumes a premelt, no-phase-change heating scenario. This could be extended by incorporating a moving solid–liquid boundary, for example, through a phase-field or level-set formulation coupled to the heat diffusion equation.[50,51] Nevertheless, although the present model is limited to the premelt regime, a spatially uniform temperature field at the onset of transition ensures that the transition threshold is reached simultaneously across the sample, reducing the risk of under-warmed regions that could fall below the critical warming rate and promote devitrification, while also limiting overheated regions that

https://doi.org/10.1021/acs.nanolett.6c02380
Nano Lett. XXXX, XXX, XXX−XXX

could damage the specimen. Because the optimization framework is differentiable, robustness to fabrication tolerances, alignment errors, and refractive index uncertainty can be incorporated directly into the optimization objective. More broadly, MetaHeat complements the efforts to use structured photonic materials for thermal management, including radiative cooling coatings, selective emitters, and inverse-designed multilayer or composite structures.[52,53] Looking forward, the ability to structure light for controlled heating in optically complex and heterogeneous media could enable new approaches to microscale thermal management, photothermal therapies, and materials processing and manufacturing.

■ ASSOCIATED CONTENT

Data Availability Statement

Additional supporting data are available on Zenodo (10.5281/zenodo.21397122).

Supporting Information

The Supporting Information is available free of charge at https://pubs.acs.org/doi/10.1021/acs.nanolett.6c02380.

Evolution of the metasurface phase profile, the temperature histogram, and the target temperature field during wavefront optimization (MP4)

Derivation of the Fourier-domain transient heat diffusion equation and treatment of boundary conditions; effect of extinction coefficient on achievable heating uniformity; validation of the wave propagation model against FDTD simulations; validation of the heat diffusion model against finite-difference simulations; example metasurface implementation and validation; summary of metasurface optimization results, analysis of sensitivity to position, size, refractive index, multistart optimization and sensitivity to initial guess; hardware benchmarks (PDF)

■ AUTHOR INFORMATION

Corresponding Author

Ognjen Ilic − *Department of Mechanical Engineering, University of Minnesota, Minneapolis, Minnesota 55455, United States*; orcid.org/0000-0001-8651-7438; Email: ilic@umn.edu

Authors

Homayra T. Mumu − *Department of Chemical Engineering and Materials Science, University of Minnesota, Minneapolis, Minnesota 55455, United States*

Yujie Luo − *Department of Mechanical Engineering, University of Minnesota, Minneapolis, Minnesota 55455, United States*

Joseph Kangas − *Department of Mechanical Engineering, University of Minnesota, Minneapolis, Minnesota 55455, United States*

John Bischof − *Department of Mechanical Engineering, University of Minnesota, Minneapolis, Minnesota 55455, United States*; orcid.org/0000-0001-6726-7111

Cari Dutcher − *Department of Mechanical Engineering and Department of Chemical Engineering and Materials Science, University of Minnesota, Minneapolis, Minnesota 55455, United States*; orcid.org/0000-0003-4325-9197

Complete contact information is available at: https://pubs.acs.org/10.1021/acs.nanolett.6c02380

Author Contributions

[†]H.T.M. and Y.L. contributed equally.

Notes

The authors declare no competing financial interest.

■ ACKNOWLEDGMENTS

The authors acknowledge support from the Office of Naval Research under Grant N00014-23-1-2627 and the Defense Advanced Research Projects Agency under Grant D24AP00310-00. J.K. and J.B. acknowledge support from the National Science Foundation Engineering Research Center under Grant EEC-1941543.

■ REFERENCES

(1) Wilson, L. O.; Celler, G. K.; Trimble, L. E. Deep melting of silicon wafers. *J. Electrochem. Soc.* **1986**, *133*, 383−389.

(2) Wang, Y.-G.; Hou, S.-P.; Lv, Q.-C. Research progress on the application of high-power laser cutting, welding, and drilling. *Front. Phys.* **2025**, *13*, DOI: DOI: 10.3389/fphy.2025.1595077.

(3) Gao, B.; Zhao, H.; Peng, L.; Sun, Z. A review of research progress in Selective Laser Melting (SLM). *Micromachines (Basel)* **2023**, *14*, 57.

(4) Algorri, J. F.; López-Higuera, J. M.; Rodríguez-Cobo, L.; Cobo, A. Advanced light source technologies for photodynamic therapy of skin cancer lesions. *Pharmaceutics* **2023**, *15*, 2075.

(5) Kim, Y.; Kang, H. W. Multi-lens array (MLA)-assisted power-modulated photothermal therapy for enhanced cancer treatment. *IEEE J. Sel. Top. Quantum Electron.* **2023**, *29*, 1−8.

(6) Kim, H.; Pyo, H.; Kim, H.; Kang, H. W. Multi-lens arrays (MLA)-assisted photothermal effects for enhanced fractional cancer treatment: Computational and experimental validations. *Cancers (Basel)* **2021**, *13*, 1146.

(7) Boechat, A.; Torezan, L.; Osório, N. In *Daily Routine in Cosmetic Dermatology*, Issa, M. C. A., Tamura, B., Eds.; Springer International Publishing: Cham, 2017; pp 273−318, DOI: DOI: 10.1007/978-3-319-12589-3_30.

(8) Kim, M. M.; Darafsheh, A. Light sources and dosimetry techniques for photodynamic therapy. *Photochem. Photobiol.* **2020**, *96*, 280−294.

(9) Tan, Y.; Sun, S.; Chen, D.; Qiu, H.; Zeng, J.; Wang, Y.; Zhao, H.; Gu, Y. Light delivery device modelling for homogenous irradiation distribution in photodynamic therapy of non-spherical hollow organs. *Photodiagnosis Photodyn. Ther.* **2021**, *34*, 102320.

(10) Thamm, O. C.; Eschborn, J.; Schäfer, R. C.; Schmidt, J. Advances in modern microsurgery. *J. Clin. Med.* **2024**, *13*, 5284.

(11) Bissoyi, A.; Braslavsky, I. Adherent cell thawing by infrared radiation. *Cryobiology* **2021**, *103*, 129−140.

(12) Yoon, J.; Lee, M.; Lee, K.; Kim, N.; Kim, J. M.; Park, J.; Yu, H.; Choi, C.; Heo, W. D.; Park, Y. Optogenetic control of cell signaling pathway through scattering skull using wavefront shaping. *Sci. Rep.* **2015**, *5*, 13289.

(13) Packer, A. M.; Russell, L. E.; Dalgleish, H. W. P.; Häusser, M. Simultaneous all-optical manipulation and recording of neural circuit activity with cellular resolution in vivo. *Nat. Methods* **2015**, *12*, 140−146.

(14) Hopkins, J. B.; Badeau, R.; Warkentin, M.; Thorne, R. E. Effect of common cryoprotectants on critical warming rates and ice formation in aqueous solutions. *Cryobiology* **2012**, *65*, 169−178.

(15) Liu, Y.; Kangas, J.; Wang, Y.; Khosla, K.; Pasek-Allen, J.; Saunders, A.; Oldenburg, S.; Bischof, J. Photothermal conversion of gold nanoparticles for uniform pulsed laser warming of vitrified biomaterials. *Nanoscale* **2020**, *12*, 12346−12356.

(16) Zhan, L.; Guo, S.-Z.; Kangas, J.; Shao, Q.; Shiao, M.; Khosla, K.; Low, W. C.; McAlpine, M. C.; Bischof, J. Conduction cooling and plasmonic heating dramatically increase droplet vitrification volumes for cell cryopreservation. *Adv. Sci. (Weinh.)* **2021**, *8*, 2004605.

(17) Khosla, K.; Zhan, L.; Bhati, A.; Carley-Clopton, A.; Hagedorn, M.; Bischof, J. Characterization of laser gold nanowarming: A platform for millimeter-scale cryopreservation. *Langmuir* **2019**, *35*, 7364−7375.

(18) Chen, Q.; Ren, Y.; Yin, Y.; Qi, H. Anisotropic scattering characteristics of nanoparticles in different morphologies: improving the temperature uniformity of tumors during thermal therapy using forward scattering. *Biomed. Opt. Express* **2021**, *12*, 893−906.

(19) Alvarez, C.; Berrospe-Rodriguez, C.; Wu, C.; Pasek-Allen, J.; Khosla, K.; Bischof, J.; Mangolini, L.; Aguilar, G. Photothermal heating of titanium nitride nanomaterials for fast and uniform laser warming of cryopreserved biomaterials. *Front. Bioeng. Biotechnol.* **2022**, *10*, 957481.

(20) Chen, Y.-S.; Hung, Y.-C.; Liau, I.; Huang, G. S. Assessment of the in vivo toxicity of gold nanoparticles. *Nanoscale Res. Lett.* **2009**, *4*, 858−864.

(21) Riley, R. S.; Day, E. S. Gold nanoparticle-mediated photothermal therapy: applications and opportunities for multimodal cancer treatment: Gold nanoparticle-mediated photothermal therapy. *Wiley Interdiscip. Rev. Nanomed. Nanobiotechnol.* **2017**, *9*, No. e1449.

(22) Wang, X.; Liu, C.; Qiao, L.; Zhou, J.; Bai, Y.; Sun, J. Imaging with high resolution and wide field of view based on an ultrathin microlens array. *Phys. Rev. Appl.* **2024**, *21*, 034035.

(23) Wippermann, F.; Zeitner, U.-D.; Dannberg, P.; Bräuer, A.; Sinzinger, S. Beam homogenizers based on chirped microlens arrays. *Opt. Express* **2007**, *15*, 6218−6231.

(24) Sales, T. R. M. Structured microlens arrays for beam shaping. *Opt. Eng.* **2003**, *42*, 3084.

(25) Wu, R.; Zheng, Z.; Li, H.; Liu, X. Optimization design of irradiance array for LED uniform rectangular illumination. *Appl. Opt.* **2012**, *51*, 2257−2263.

(26) Wang, K.; Wu, D.; Qin, Z.; Chen, F.; Luo, X.; Liu, S. New reversing design method for LED uniform illumination. *Opt. Express* **2011**, *19* (Suppl4), A830−40.

(27) Ma, D.; Feng, Z.; Liang, R. Freeform illumination lens design using composite ray mapping. *Appl. Opt.* **2015**, *54*, 498.

(28) Li, Z.; Yu, S.; Lin, L.; Tang, Y.; Ding, X.; Yuan, W.; Yu, B. Energy feedback freeform lenses for uniform illumination of extended light source LEDs. *Appl. Opt.* **2016**, *55*, 10375−10381.

(29) Mao, X.; Li, H.; Han, Y.; Luo, Y. Polar-grids based source-target mapping construction method for designing freeform illumination system for a lighting target with arbitrary shape. *Opt. Express* **2015**, *23*, 4313−4328.

(30) Ding, Y.; Liu, X.; Zheng, Z.-R.; Gu, P.-F. Freeform LED lens for uniform illumination. *Opt. Express* **2008**, *16*, 12958−12966.

(31) Zhang, Z.; You, Z.; Chu, D. Fundamentals of phase-only liquid crystal on silicon (LCOS) devices. *Light Sci. Appl.* **2014**, *3*, e213−e213.

(32) Yang, Y.; Forbes, A.; Cao, L. A review of liquid crystal spatial light modulators: devices and applications. *Opto-Electron Sci.* **2023**, *2*, 230026.

(33) Durdevic, L.; Robert, H. M. L.; Wattellier, B.; Monneret, S.; Baffou, G. Microscale temperature shaping using spatial light modulation on gold nanoparticles. *Sci. Rep.* **2019**, *9*, 4644.

(34) Ayoub, A. B.; Psaltis, D. High speed, complex wavefront shaping using the digital micro-mirror device. *Sci. Rep.* **2021**, *11*, 18837.

(35) Conkey, D. B.; Caravaca-Aguirre, A. M.; Piestun, R. High-speed scattering medium characterization with application to focusing light through turbid media. *Opt. Express* **2012**, *20*, 1733−1740.

(36) Bifano, T. MEMS deformable mirrors. *Nat. Photonics* **2011**, *5*, 21−23.

(37) Madec, P.-Y. In *Adaptive Optics Systems III*, ed. by Ellerbroek, B. L.; Marchetti, E.; Véran, J.-P., SPIE: 2012, DOI: DOI: 10.1117/12.924892.

(38) Hornbeck, L. J. In *Spatial Light Modulators and Applications III*, ed. by Efron, U., SPIE: 1990, DOI: DOI: 10.1117/12.962188.

(39) Schmidt, S.; Tiess, T.; Schröter, S.; Hambach, R.; Jäger, M.; Bartelt, H.; Tünnermann, A.; Gross, H. Wave-optical modeling beyond the thin-element-approximation. *Opt. Express* **2016**, *24*, 30188−30200.

(40) Gebremedhin, A. H.; Walther, A. An introduction to algorithmic differentiation. *Wiley Interdiscip. Rev. Data Min. Knowl. Discovery* **2020**, *10*, DOI: DOI: 10.1002/widm.1334.

(41) Margossian, C. C. A review of automatic differentiation and its efficient implementation. *Wiley Interdiscip. Rev. Data Min. Knowl. Discovery* **2019**, *9*, No. e1305.

(42) Paszke, A. et al. In *Advances in Neural Information Processing Systems*, ed. by Wallach, H.; Larochelle, H.; Beygelzimer, A.; d'Alché-Buc, F.; Fox, E.; Garnett, R., Curran Associates, Inc.: 2019; Vol. 32.

(43) Bradbury, J.; Frostig, R.; Hawkins, P.; Johnson, M. J.; Katariya, Y.; Leary, C.; Maclaurin, D.; Necula, G.; Paszke, A.; VanderPlas, J.; Wanderman-Milne, S.; Zhang, Q. JAX.: *composable transformations of Python+NumPy programs*, version 0.3.13, 2018.

(44) Bezanson, J.; Edelman, A.; Karpinski, S.; Shah, V. B. Julia: A fresh approach to numerical computing. *SIAM Rev. Soc. Ind. Appl. Math.* **2017**, *59*, 65−98.

(45) Yun, J.; Chae, D.; So, S.; Lim, H.; Noh, J.; Park, J.; Kim, N.; Park, C.; Lee, H.; Rho, J. Optimally designed multimaterial microparticle−polymer composite paints for passive daytime radiative cooling. *ACS Photonics* **2023**, *10*, 2608−2617.

(46) Keawmuang, H.; Badloe, T.; Lee, C.; Park, J.; Rho, J. Inverse design of colored daytime radiative coolers using deep neural networks. *Sol. Energy Mater. Sol. Cells* **2024**, *271*, 112848.

(47) Kleinhans, F. W.; Jin, B.; Paredes, E.; Mazur, P. 093 Ultra rapid warming of cryo samples using an IR laser pulse. *Cryobiology* **2013**, *67*, 424.

(48) Kleinhans, F. W.; Mazur, P. Physical parameters, modeling, and methodological details in using IR laser pulses to warm frozen or vitrified cells ultra-rapidly. *Cryobiology* **2015**, *70*, 195−203.

(49) Oskooi, A. F.; Roundy, D.; Ibanescu, M.; Bermel, P.; Joannopoulos, J. D.; Johnson, S. G. Meep: A flexible free-software package for electromagnetic simulations by the FDTD method. *Comput. Phys. Commun.* **2010**, *181*, 687−702.

(50) Chen, S.; Merriman, B.; Osher, S.; Smereka, P. A simple level set method for solving Stefan problems. *J. Comput. Phys.* **1997**, *135*, 8−29.

(51) Boettinger, W. J.; Warren, J. A.; Beckermann, C.; Karma, A. Phase-field simulation of solidification. *Annu. Rev. Mater. Res.* **2002**, *32*, 163−194.

(52) So, S.; Yun, J.; Ko, B.; Lee, D.; Kim, M.; Noh, J.; Park, C.; Park, J.; Rho, J. Radiative cooling for energy sustainability: From fundamentals to fabrication methods toward commercialization. *Adv. Sci. (Weinh.)* **2024**, *11*, No. e2305067.

(53) Keawmuang, H.; et al. Recent advances in radiative cooling: From fundamentals to commercial applications. *ACS Appl. Mater. Interfaces* **2026**, *18*, 21363−21423.

https://doi.org/10.1021/acs.nanolett.6c02380
Nano Lett. XXXX, XXX, XXX−XXX